Highly Efficient Broadband Pyramidal Horn Antenna With Integrated H-Plane Power Division

Charalampos Stoumpos, Jean-Philippe Fraysse, George Goussetis, Cebrian Garcia Gonzalez, Ronan Sauleau, Hervé Legay

Highly Efficient Broadband Pyramidal Horn Antenna with Integrated H-Plane Power Division

Charalampos Stoumpos, Jean-Philippe Fraysse, George Goussetis, *Senior Member*, *IEEE*, Cebrián García González, Ronan Sauleau, *Fellow*, *IEEE* and Hervé Legay

***Abstract*—The concept and development of a highly efficient pyramidal horn is described. The radiating element comprises a rectangular radiating aperture fed by two smaller flared square waveguide sections via a bi-furcated H-plane surface discontinuity. For the simultaneous feeding of the 2-port radiating element, the total antenna includes a compact H-plane power divider. Properly weighted TE_{n0} modes ($n \in N^*$) are excited at the output of the two flared waveguide sections. The bifurcation is responsible for the recombination of the incoming fields. The low-dispersive modal coupling coefficients (or transmission coefficients of the bifurcation's generalized scattering matrix) between the excitation and the aperture modes enable the broadband realization of the targeted aperture modal content. The common waveguide section is responsible for the phase alignment of the aperture modes. The design method targets a pre-optimized model which approximates the amplitude of the aperture modes TE_{m0} (m = 1, 3, 5, …) in the order of $1/m$ and minimises their relative phase difference. Finally, maximum aperture efficiency can be achieved by fine tuning and with low computational complexity. Design principles are given and illustrated by means of an example involving an antenna with aperture size of about $2.8\lambda_0 \times 1.4\lambda_0$ (λ_0 being the free-space wavelength at the central frequency of operation). The antenna exhibits aperture efficiency levels above 95% over the entire Ku-Tx band (10.7 – 12.75 GHz), as well as a compact profile ($4.1\lambda_0$). The measured results of a prototype manufactured through milling verify experimentally the numerically predicted performance.**

***Index Terms*--Aperture antenna, pyramidal horn, aperture efficiency, mode-matching, integrated power division.**

I. Introduction

HORN ANTENNAS are widely used in various microwave and millimeter wave applications such as satellite missions and measurement systems [1]. The main beneficial features of this type of radiating element lie on their low losses, moderate/high directivity and strong robustness. For space missions, an important challenge deals with the design of innovative horn architectures with simultaneously a low profile and high aperture efficiency.

A rectangular horn operating in only the TE_{10} mode has a maximum aperture efficiency of 81% [2]. This stems from the not totally uniform field distribution in amplitude and phase across the aperture as the aperture theory dictates [3]. However, when several high-order modes are included, higher efficiency can be obtained.

Manuscript received April 01, 2021; revised June 04 and July 15, 2021; accepted July 30, 2021. This work was supported by the European Union's Horizon 2020 research and innovation program under the Marie Skłodowska-Curie Grant Agreement REVOLVE No. 722840.

C. Stoumpos is with the School of Engineering and Physical Sciences, Heriot-Watt University, Edinburgh EH14 4AS, U.K. and also with the Research and Development Department, Thales Alenia Space, 31037 Toulouse, France (e-mail: cs118@hw.ac.uk, haris_stou@hotmail.com).

J. P. Fraysse and H. Legay are with the Research and Development Department, Thales Alenia Space, 31037 Toulouse, France. (e-mail: {jean-philippe.fraysse; herve.legay}@thalesaleniaspace.com).

G. Goussetis is with the School of Engineering and Physical Sciences, Heriot-Watt University, Edinburgh EH14 4AS, U.K. (e-mail: g.goussetis@hw.ac.uk).

Cebrián García González is with Idonial Centro Tecnológico, 33203 Gijón, Asturias, Spain (e-mail: cebrian.garcia@idonial.com).

R. Sauleau is with the Univ Rennes, CNRS, Institut d'Electronique et des Technologies du numéRique (IETR) — UMR CNRS 6164, F-35000 Rennes, France (e-mail: ronan.sauleau@univ-rennes1.fr).

Digital Object Identifier xxx/TAP.2021.xxx

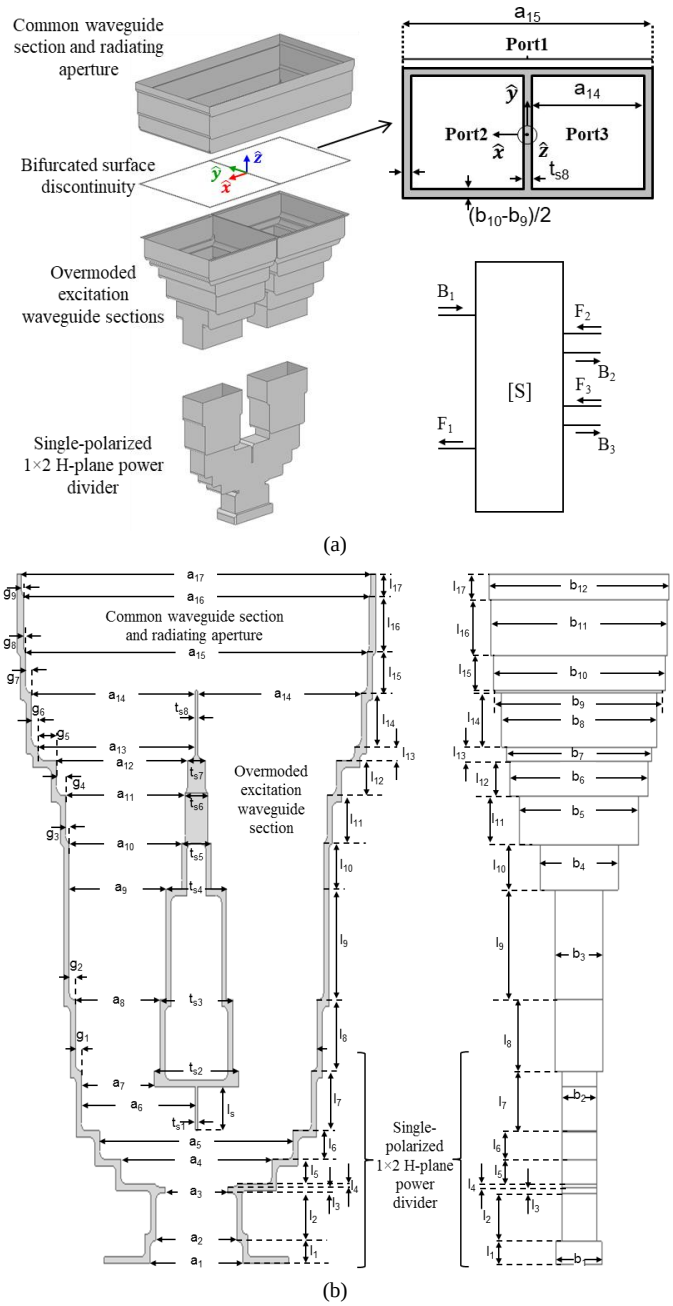

Fig. 1. Layout and geometry of the proposed Ku-Tx band pyramidal horn antenna: (a) exploded view of the layout with the four individual components (left) and geometry of the bifurcated discontinuity (upper right) with its schematic block diagram representing its generalized scattering matrix (lower right), (b) side cut-view with dimensional variables of the mechanical model.

The aperture efficiency maximization of single-polarized horns has been the subject of investigation for many years. Techniques for the gain or radiation improvement of horns refer to dielectric or metamaterial lens on the horn aperture [4]-[8], iron baffles or slow-wave structures inside the horn [9]-[12], as well as optimization of

the horn's profile which constitutes the state-of-the-art [13]-[16]. Particularly, *Bird et al.* [13], showed that profiled single-polarized square horns achieve aperture efficiencies close to 100% for a bandwidth of up to 8% and apertures ranging from $1.25\lambda_0 \times 1.25\lambda_0$ to $3\lambda_0 \times 3\lambda_0$. Their profile is compact, they are simple to fabricate and in satellite applications are preferred against dielectric horns due to their purely metallic structure. In addition, *Bhattacharyya et al.* [16], proved that for obtaining high aperture efficiency in square horns, only TE_{m0} modes (m = 1, 3, 5, …) in amplitudes approximately 1/m and equal phase should be excited on the aperture.

In this paper we propose a novel technique for the design of broadband and highly efficient H-plane pyramidal rectangular aperture horn antennas with the larger dimension of the aperture being at least $2\lambda_0$. A visually similar (multi-access) horn antenna can be found in [17]; however, its operation is completely different. It can address large apertures and dual-polarization, while 97% aperture efficiency is also reported.

The proposed method is illustrated by the design of a transmit Ku-band (10.7-12.75 GHz) horn with aperture size of about $2.8\lambda_0 \times 1.4\lambda_0$; its geometry is shown in Fig. 1. The total antenna integrates an H-plane waveguide power divider feeding two mirror-symmetric and asymmetrically flared waveguide sections which end up to overmoded cross-sections. The appropriate design of these sections excites weighted modes in the form of TE_{n0}, $n \in N^*$, which in turn excite a bi-furcated waveguide surface discontinuity. Due to the low-dispersion of the bifurcation's modal transmission coefficients between the two excitation waveguides and the common waveguide, the proposed H-plane pyramidal horn antenna manages to realize the targeted aperture modal content over a wide frequency bandwidth. Between the bifurcated discontinuity and the final radiating aperture, a common waveguide section is responsible for the phase alignment of the propagating aperture modes which maximize the antenna gain and hence its aperture efficiency. This type of radiating element manages to achieve a modal distribution close to the desired one over a broad frequency bandwidth. The proposed antenna achieves aperture efficiency values above 95% for a frequency bandwidth larger than 20%. At the same time, the horn maintains an axial profile about $4.1\lambda_0$ and its mechanical layout and hence fabrication process is simple. As a result, the proposed horn antenna constitutes an appealing alternative to the profiled multimodal horns.

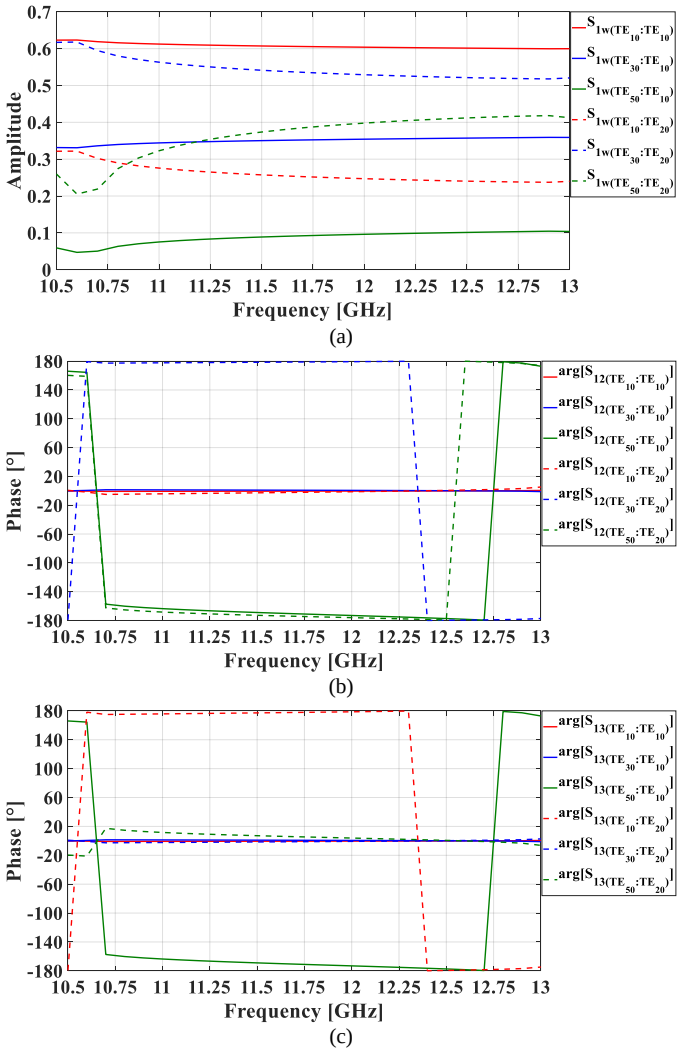

Fig. 2. Bifurcated waveguide surface discontinuity's transmission coefficients among the modes TE_{10}, TE_{20} of the two excitation waveguides (ports w = 2, 3) and TE_{10}, TE_{30} and TE_{50} of the common waveguide (port 1). (a) Amplitude. (b) Phase at port 2. (c) Phase at port 3.

II. Design Principles

The conventional approach used for the design of high-efficiency rectangular or square single-polarized horns is based on the aperture modes TE_{m0} (m =1, 3, 5, …) with approximate amplitudes of 1/m and equal phase [16]. This is close to optimum (tends asymptotically to 100% as $m \to \infty$) when mismatch and mode coupling at the aperture is small [13], [14]. For profiled horns, this distribution is achieved by virtue of appropriate discontinuities which control the aperture modal content. In this work, we propose a different approach.

The design methodology of the presented radiating element begins with the above-mentioned modal distribution. The process exploits two stages. In the first stage we consider the antenna as a 3-port structure terminated at the corresponding waveguide ports. In this stage, we first adjust for the desired power distribution across the three modes at the interface of the bi-furcated discontinuity with the common waveguide aperture. The phase alignment is then achieved in a second stage by tuning the finite length of the common waveguide region. Thereby, we obtain an initial and pre-optimized model which is later finely tuned for optimum performance [13].

A. Bi-furcated Surface Waveguide Discontinuity

The bi-furcated surface waveguide discontinuity is the interface between the two excitation waveguides and the common waveguide acting as a mode converter. Its geometry is defined in the upper right part of Fig. 1(a). The design focuses on the modal transmission between the common rectangular waveguide and each of the two smaller ones. We used the Mode-Matching method [14], [18]-[19] for the calculation of this discontinuity's Generalized Scattering Matrix (GSM) represented as a 3-port network and depicted in the lower right part of Fig. 1(a). F_w (F_2, F_3) is the forward input modal voltage vector feeding the bi-furcation and B_w (B_2, B_3) the backscattered modal voltage vector. F_1 is the forward and B_1 the backscattered modal voltage vector at the common port of the bi-furcation.

Thereafter, we proceed with the study of the modal coupling coefficients at the bi-furcation $S_{1w(h_{m0}:h_{i0})}$, with w=1,2 being the excitation waveguides index, m=1,3,5 the common waveguide modes index and i=1,2 the excitation waveguide modes index. With reference to Fig. 1(a), the geometry is thus defined by the dimensions of the excitation waveguides (a_{14}, b_9) and the common waveguide (a_{15}, b_{10}), the gap between each pair of them as well as the boundary of the common waveguide [g_7=t_{s8}=(a_{15}-2a_{14})/3 and (b_{10}-b_9)/2]. The magnitude of scattering parameters between port 1 and the two excitation ports (w=2, 3) is identical. Without loss of generality, for the analysis and the example design in the remaining of this paper the reference polarization is considered along y-axis. For this analysis the common waveguide aperture edge is a_{15}=68mm. This is approximately equal to $2.65\lambda_0$, such that it reaches $2.8\lambda_0$ at the

radiating aperture after slight flaring (a_{16}=71.2 mm, a_{17}=72 mm). The aperture size allows the propagation of the TE_{50} mode over the total Ku-Tx band.

Fig. 2(a) shows the amplitude of the bi-furcated discontinuity's transmission coefficients among the modes TE_{10} and TE_{20} from the excitation waveguides w=2, 3 and the modes TE_{10}, TE_{30} and TE_{50} of the common waveguide (port 1). The dominant TE_{10} mode from the excitation waveguides couples to the dominant TE_{10} mode of the common aperture [solid red line] at normalized levels of about 0.62, while to the mode TE_{30} of the common aperture mode [$S_{1w(TE_{30}:TE_{10})}$, solid blue line] at levels of about 0.35 [Fig. 2(b)]. On this basis, the relative strength of the TE_{30} mode in the common aperture would be higher than what is posed by the condition $1/m$ (m = 1, 3, …), which in turn would compromise the aperture efficiency. Fig. 2(b) shows also the bi-furcation's coupling phase of the TE_{10} and TE_{20} modes from the excitation waveguide 2 to the three propagating modes that contribute to the maximum directivity. Fig. 2(c) shows the bi-furcation's coupling phase from the excitation waveguide 3.

The mode TE_{20} from the waveguide 2 couples 180˚ out of phase to the common waveguide mode TE_{30}, as illustrated by the two blue lines in Fig. 2(b). Besides, this is not true for the waveguide 3 [the two blue lines in Fig. 2(c) are in phase]. Therefore, if the mode TE_{20} in the waveguide 3 could be excited 180˚ out of phase, the common aperture mode TE_{30} could be modulated properly to be compliant with the desired level. Besides, the common waveguide mode TE_{50} couples to the excitation modes TE_{10} and TE_{20} (green lines) at levels of about 0.1 and 0.4, respectively. However, it couples 180˚ out of phase [except for $S_{13(TE_{50}:TE_{20})}$, dashed green line]. Thereby, the correction of the common mode TE_{50} phase shift is essentially the reason we need to include the upper common waveguide section.

Thereafter, assuming that the two excitation modes are only the TE_{10} and TE_{20} and suppressing the common waveguide reflection coefficient matrix as it contributes to the power normalization of each mode at the common waveguide, the non-normalized modal vector at the bifurcated discontinuity's common waveguide can be written as:

$$\begin{bmatrix} F_1^{h_{10}} \\ F_1^{h_{30}} \\ F_1^{h_{50}} \end{bmatrix} = \frac{1}{\sqrt{2}} \begin{bmatrix} \sum_{w=2}^{3} \left(\begin{matrix} |h_{10}^{\text{in}}| \cdot e^{j\varphi_{w,h_{10}^{\text{in}}}} \cdot |S_{1w(h_{10}:h_{10})}| \cdot e^{j\varphi_{S_{1w(h_{10}:h_{10})}}} + \\ |h_{20}^{\text{in}}| \cdot e^{j\varphi_{w,h_{20}^{\text{in}}}} \cdot |S_{1w(h_{10}:h_{20})}| \cdot e^{j\varphi_{S_{1w(h_{10}:h_{20})}}} \end{matrix} \right) \\ \sum_{w=2}^{3} \left(\begin{matrix} |h_{10}^{\text{in}}| \cdot e^{j\varphi_{w,h_{10}^{\text{in}}}} \cdot |S_{1w(h_{30}:h_{10})}| \cdot e^{j\varphi_{S_{1w(h_{30}:h_{20})}}} + \\ |h_{20}^{\text{in}}| \cdot e^{j\varphi_{w,h_{20}^{\text{in}}}} \cdot |S_{1w(h_{30}:h_{20})}| \cdot e^{j\varphi_{S_{1w(h_{30}:h_{20})}}} \end{matrix} \right) \\ \sum_{w=2}^{3} \left(\begin{matrix} |h_{10}^{\text{in}}| \cdot e^{j\varphi_{w,h_{10}^{\text{in}}}} \cdot |S_{1w(h_{50}:h_{10})}| \cdot e^{j\varphi_{S_{1w(h_{50}:h_{10})}}} + \\ |h_{20}^{\text{in}}| \cdot e^{j\varphi_{w,h_{20}^{\text{in}}}} \cdot |S_{1w(h_{50}:h_{20})}| \cdot e^{j\varphi_{S_{1w(h_{50}:h_{20})}}} \end{matrix} \right) \end{bmatrix} \quad (1)$$

The $1/\sqrt{2}$ factor assures that the total power of the 3-port network is normalized to 1. The terms $h_{10}^{\text{in}} = |h_{10}^{\text{in}}| \cdot e^{j\varphi_{w,h_{10}^{\text{in}}}}$, $|h_{20}^{\text{in}}| \cdot e^{j\varphi_{w,h_{20}^{\text{in}}}}$ in polar form refer to the two excitation modal voltage vectors (F_w, w=2,3) excited by the two input waveguides. Likewise, the terms $S_{1w(h_{10}:h_{10})}$, $S_{1w(h_{10}:h_{20})}$ presented as well in polar form in eq. (1) refer to the modal coupling coefficients of the bi-furcation's GSM (see Fig. 2). In addition, each second term of every summation in eq. (1) will be suppressed and there will no longer be a contribution from the mode TE_{20}, if and only if $\varphi_{w,h_{20}^{\text{in}}}$ is the same $\forall$ w=2, 3. This occurs by the 180˚ phase inversion of the coupling mode between the mode TE_{20} of the two excitation waveguides (2, 3) and the common waveguide modes TE_{10} and TE_{30} at the bifurcated surface discontinuity [180˚ phase difference between the red and blue dashed lines of Figs. 2(b) and 3(c)]. In other words, the excitation waveguides should be designed so as to comply with the following relation:

$$\left|\varphi_{2,h_{20}^{\text{in}}} - \varphi_{3,h_{20}^{\text{in}}}\right| = 180^\circ \Rightarrow e^{j\varphi_{2,h_{20}^{\text{in}}}} = -e^{j\varphi_{3,h_{20}^{\text{in}}}} \quad (2)$$

B. Excitation Waveguide Sections and the H-Plane Power Divider

The design of the two excitation waveguide sections is driven by the conditions defined from the study of the bi-furcation. These refer to the generation of the mode TE_{20} with specific amplitude [eq. (1)] as well as the 180° inversion of this mode at waveguide 3 [eq. (2)].

Therefore, the two overmoded excitation waveguide sections were designed [19] with lateral displacements to each waveguide discontinuity as well as with a mirror-symmetry with respect to each other. The first feature ensures the generation of the TE_{20} mode and the second its phase inversion by 180° at the port 3 [eq. (2)].

Fig. 3 illustrates the modal solutions of the excitation waveguide sections. As it can be identified from Fig. 3(a), the modal ratio $|h_{20}^{\text{in}}|/|h_{10}^{\text{in}}|$ is in the order of about 0.25 and from Fig. 3(b), the relative phase difference between the excitation mode TE_{10} (same for both excitation ports 2, 3) and TE_{20} (180° different between the two excitation ports 2, 3) $\Delta_{\varphi_{w,h_{10}^{\text{in}}} - \varphi_{2,h_{20}^{\text{in}}}}$ (black solid line) is around -50˚. These two values have been defined as a pair of solutions to eq. (1) subject to the aperture modal voltages defined by the condition $1/m$ (m = 1, 3, …). The input reflection coefficient [Fig. 3(a)] remains below the level of 0.15 (-16 dB) and the excitation of the undesired aperture higher order modes (not shown for brevity) maintains low levels as well (maximum value of -19dB for the mode TM_{12}).

Afterwards, the common waveguide section has been designed and optimized [19] so that the phase of the common waveguide modes can be corrected. This common waveguide section was designed with two supplementary discontinuities. Therefore, the aperture modal vector ($F_{m0}^{\text{ap}} = \text{TE}_{m0}^{\text{ap}}$, with m = 1, 3, 5 being the aperture mode index) is substantially the modal vector just after the bi-furcation excited by the two excitation waveguide sections [F_1^{m0} from eq. (1)] and multiplied by the scattering matrix of the common waveguide section which will modify the phase of the propagating modes F_1^{m0}.

The resulting structure is a 2-port radiating element (the structure of Fig. 1 without the H-plane power divider) which achieves aperture efficiency levels above 90% over the bandwidth of interest. Next, we

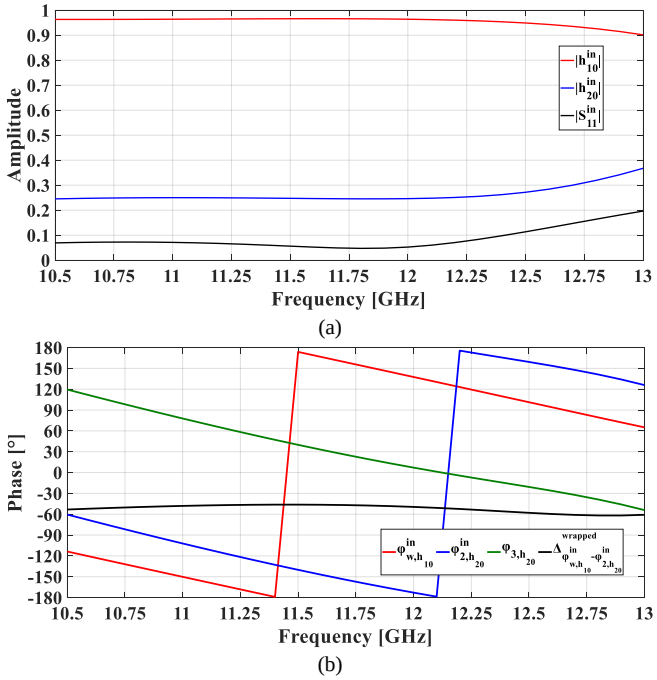

Fig. 3. Results of the optimized input waveguide sections used as excitation to the bifurcated surface discontinuity: (a) voltage amplitude of the modes TE_{10}, TE_{20} at the output (a_{14}, b_9) and reflection coefficient at the input (a_9, b_3), (b) output phase of the modes TE_{10}, TE_{20} and relative phase difference of the TE_{10} (same for both excitation waveguides w) and TE_{20} of the waveguide 2.

proceed to a final tuning with [19] for optimum performance [13]. The design closes with the H-plane power divider which was designed and optimized using the active S-parameters of the 2-port radiating element as an impedance basis [19]. The results are presented in the next section. With reference to Fig. 1(b), the optimized dimensions of the total horn antenna's structure are:

- a_i = {19.05, 16.759, 12.99, 31.078, 39.78, 23.4, 15, 17.65, 20, 23.2, 24.65, 27, 30.75, 33.8, 70.4, 71.2, 72} mm.
- b_i = {9.525, 7.138, 9.9, 16.1, 24.65, 28.4, 30, 31.9, 34.6, 35.4, 36.2, 37} mm.
- l_i = {3.5, 7.36, 0.97, 0.46, 3.81, 4.35, 9.26, 10.97, 16.982, 7.065, 7.384, 5.35, 2.15, 8.31, 6.264, 8.6, 3.52} mm.
- g_i = {1.25, 1.25, 4.45, 1.925, 3.75, 1.4, 1.2, 0.4, 0.4} mm.
- t_{s_i} = {0.6, 17.4, 14.75, 12.4, 6, 4.55, 3.7, 0.4} mm.
- l_s = 6.729 mm & milling radii = 1.1mm

III. Modal Solutions and Measurement Results

The modal solutions of the horn antenna (TE^{ap}_{m0}) are depicted in Fig. 4. The results of Fig. 4(a) illustrate that the optimized antenna realizes with a notable agreement the targeted aperture modal voltage amplitude $1/m$ (m = 1, 3, …), which as stated is close to the optimal, over the frequency bandwidth of interest. The modal phase difference (between the aperture modes TE^{ap}_{m0}) is low, with the worst-case value being -35° [Fig. 4(b)]. The modal amplitude of the rest higher order modes remains below 0.08 (-22 dB).

The simulated electric field distribution at 11.7 GHz of the total single-polarized H-plane pyramidal horn antenna is presented in Fig. 5. In particular, Fig. 5(a) depicts the instantaneous electric field flow at the cross-sectional $\hat{x}\hat{z}$-cut view also with reference to Fig. 1. As it can be identified, the electric field arrives at the aperture plane in a uniform way or in other words its amplitude and phase present a high consistency all over the radiating aperture as illustrated respectively in Figs. 5(b) and 5(c).

Fig. 6(a) illustrates the manufactured prototype (through milling) of the proposed pyramidal horn antenna. The standard manufacturing

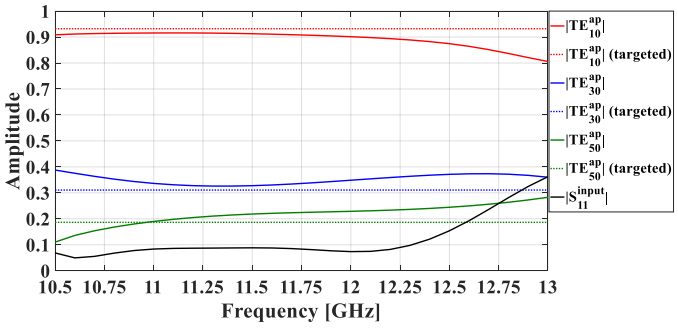

(a)

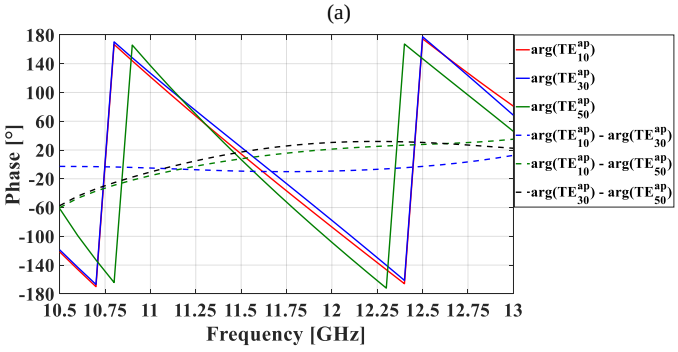

(b)

Fig. 4. Results for the optimized radiating element: (a) voltage amplitude of the aperture modes and input reflection coefficient, (b) phase and relative phase difference of the aperture modes.

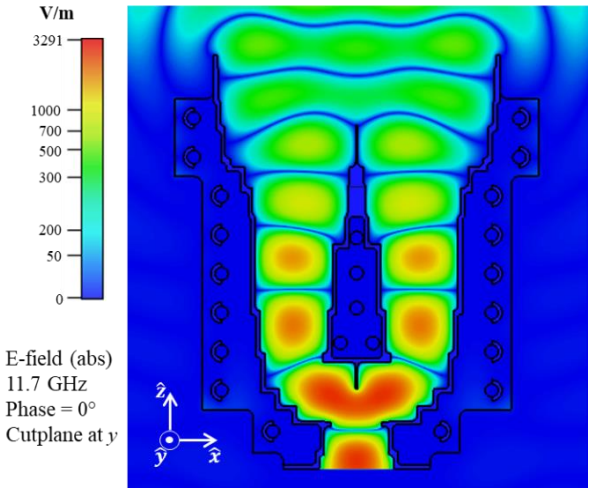

(a)

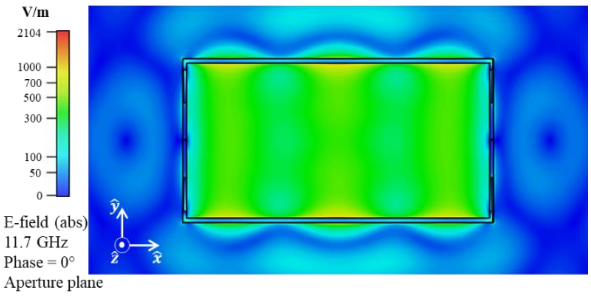

(b)

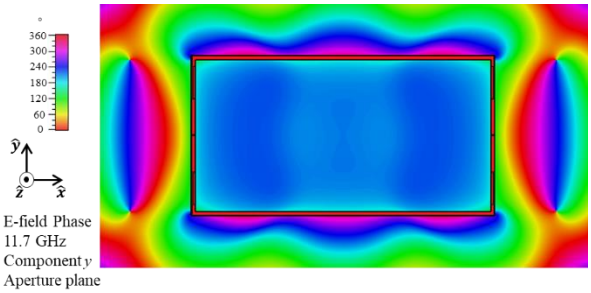

(c)

Fig. 5. Electric field at 11.7 GHz: (a) amplitude at the horn's $\hat{x}\hat{z}$-cut, (b) amplitude at the aperture plane and (c) phase at the aperture plane.

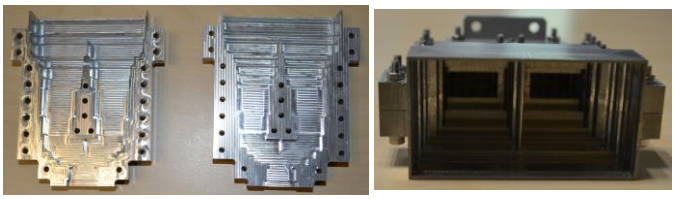

(a)

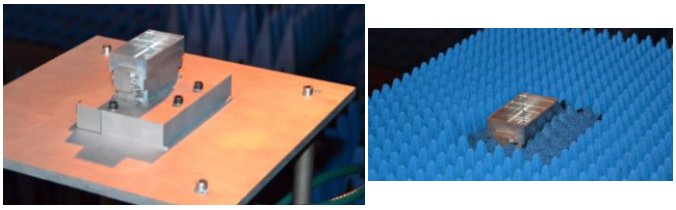

(b)

Fig. 6. Prototype and measurements of the proposed pyramidal horn antenna: (a) the two separated milled parts (left) and the assembled prototype (right), (b) the measurement setup with the metallic plate and the supporting structure (left) and the final measurement configuration with absorbers above the metallic plate (right).

tolerances and hence the fabrication precision are of the order of ±50μm. Fig. 6(b) illustrates the measurement setup in the anechoic chamber. An NSI2000 near field system has been used for the experimental verification of the horn's radiation characteristics.

The simulated S-parameters of the two individual components (the two-port radiating element and the H-plane power divider) of the total single-polarized horn are depicted in Fig. 7. It is observed that although the 2-port radiating element is not optimized for an input reflection coefficient level below -20 dB for the total band of interest, the optimization method adopted here manages to achieve a simulated response below -24 dB across this frequency band. The measured reflection coefficient of the total horn antenna is depicted in Fig. 7 as well. An excellent agreement is observed between the simulated and measured results. The measured reflection coefficient remains below -24 dB from 10.55 to 12.85 GHz.

Fig. 8(a) shows the three principal plane-cuts of the normalized co-polarized directivity patterns (and the cross-polarized at φ=45˚) of the horn antenna at the central frequency of 11.7 GHz together with the ideal case of an aperture with the same physical size illuminated uniformly (100% aperture efficiency) based on the equivalence principle [1]. High consistency between the two cases can be observed. Figs. 8(b) and 8(c) illustrate the measured and simulated directivity patterns at the lowest and highest frequency of the Ku-Tx band, respectively. An excellent agreement can be observed as well. Fig. 9 depicts the measured and simulated broadside gain and aperture efficiency across the frequency. The uncertainty of the measurements with respect to the realized gain presents a level in the order of ±0.25dB. The experimental results show that the proposed horn achieves aperture efficiency levels above 92% for a bandwidth larger than 20%. The aperture efficiency has been calculated as [1]:

$$n_{\text{Ap.Eff.}} = \frac{\lambda^2 G}{4\pi A} \tag{3}$$

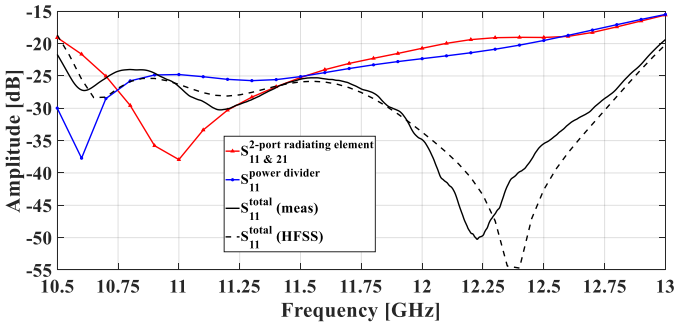

Fig. 7. The simulated S-parameters of the two-port radiating element, the H-plane power divider and the total optimized horn antenna with the measured reflection coefficient.

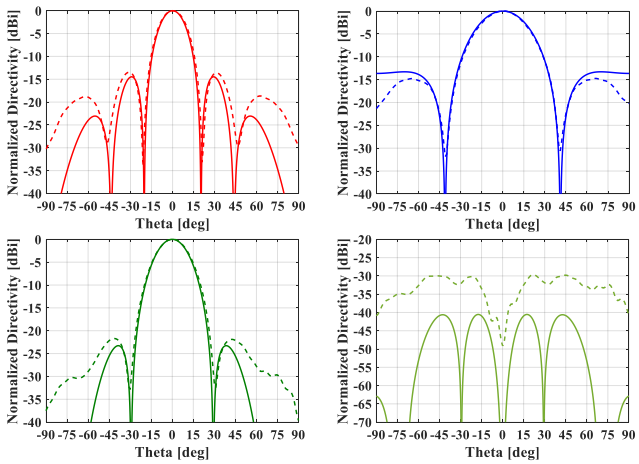

(a)

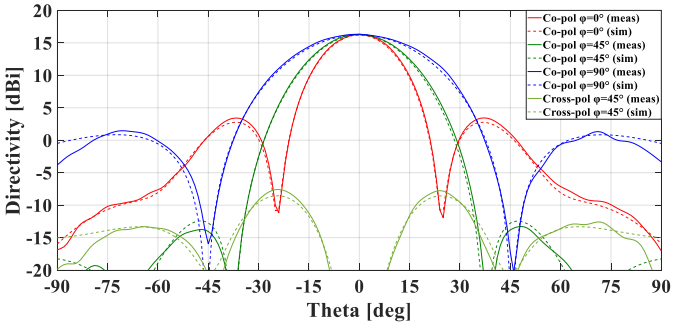

(b)

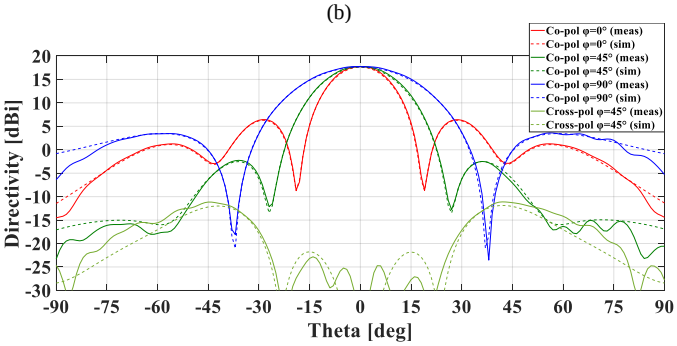

(c)

Fig. 8. Directivity radiation patterns of the horn antenna. (a) Normalized measured (dashed line) versus ideal (solid lines) patterns at φ=0˚ (upper left), φ=90˚ (upper right), φ=45˚ (lower left) and cross-pol φ=45˚ (lower right) at 11.7 GHz. (b) Measured (solid lines) and simulated (dashed lines) at 10.7 GHz. (c) Measured (solid lines) and simulated (dashed lines) at 12.75GHz.

where λ the wavelength, G the realized broadside gain and A = 0.072×0.037 m^2, the electric aperture of the radiating element. It is noted that the wall thickness of the aperture's flange has not been taken into account in A. This thickness, according to simulations, results in a gain increase of 0.08 dB (around 1.8% in aperture efficiency). Deviations between simulated and measured values are in the order of ±0.2 dB, which is less than the uncertainty levels of the measurement system (±0.25 dB). Other reasons for these discrepancies are the mechanical tolerances as well as differences between the conductivity value of the prototyped antenna and this used in simulations (25 MSiemens/meter). We also mention that the differences between simulated and measured broadside directivity across the frequency are less than ±0.15 dB. Finally, the simulated and measured maximum cross-polarization of the pyramidal horn remains below -23 dB over the total band of 10.5–13 GHz.

Table I shows the state-of-the-art high aperture efficiency horns with square or rectangular apertures. Horns based on slow wave structures achieve significant height reduction, but suffer from limited aperture efficiency [12]. Single-polarized profiled horns present aperture efficiency values above 92% over a bandwidth of 8% and for aperture sizes around $2\lambda_0 \times 2\lambda_0$ [13]. Dual-polarized profiled horns with $3\lambda_0 \times 3\lambda_0$ aperture sizes present aperture efficiency

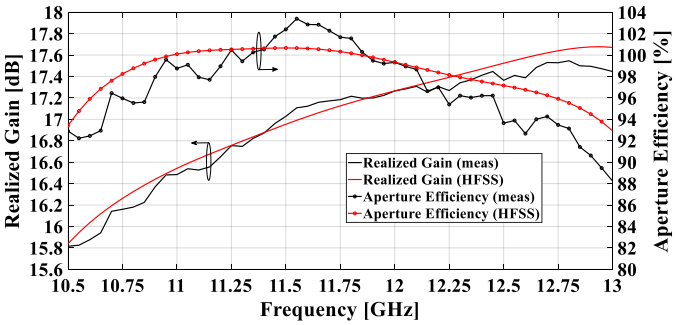

Fig. 9. Measured and simulated realized gain and aperture efficiency of the pyramidal horn antenna.

TABLE I
COMPARISON OF STATE-OF-THE-ART SQUARE AND RECTANGULAR APERTURE HIGH EFFICIENCY RADIATING ELEMENTS

Ref. →	[12]	[13]	[16]	This work
Aperture Size ($\lambda_0\times\lambda_0$)	2.5×0.57	2×2	3×3	2.8×1.4
Bandwidth (%)	30	8	20	20
Aperture Efficiency* (%)	63-83	92-97	85-90	93-99
Polarization	Single	Single	Dual	Single
Min Return Loss (dB)	15	20	25	24
Min Cross-Pol (dB)	N/A	22	N/A	23
Profile (λ_0)	2.5	3.2	7.1	4.1
Horn Antenna Type	Slow Wave	Profiled	Profiled	Multi-port

*Defined by (3) with *A* being the aperture without the flange thickness; the contribution of the aperture's flange thickness to the numerically calculated realized gain [*G* in (3)] has not been considered for fair comparison.

values between 85-90% over a bandwidth of 20% and at the cost of increased height [16]. In the comparative framework of this work, we implemented designs on optimized single-polarized rectangular aperture profiled horns with aperture sizes between $2.6\lambda_0\times1.3\lambda_0$ and $3\lambda_0\times1.5\lambda_0$. The calculated aperture efficiency levels were similar to those reported in [13] (not shown for brevity); i.e. above 94% over a bandwidth of 8% and above 91% over a bandwidth of 18%. Therefore, the proposed horn achieves higher aperture efficiency levels over a wider bandwidth without significant height penalty with respect to the state-of-the-art; the aperture efficiency is above 93% over a bandwidth of 20% and above 96% over a bandwidth of 14%.

IV. CONCLUSION

In this paper, a novel highly efficient wide bandwidth waveguide pyramidal horn has been presented. The proposed solution is an alternative to the profiled single-polarized horns, which achieve high aperture efficiencies by properly modulating their longitudinal profile. The total horn antenna utilizes an H-plane power divider which feeds two mirror-symmetric tapered waveguide sections. These sections present laterally displaced discontinuities for the generation of the mode TE_{20}. These excite in turn a bi-furcated waveguide discontinuity which recombines the input fields and leads to the radiating aperture with a common waveguide section of finite length for the phase correction of the aperture modes. The proposed method, essentially, defines a design framework by which a pre-optimized 2-port radiating element can be obtained. This is based on the conventional approach used for the design of high-efficiency rectangular or square horns where we aim at modulating the aperture modes TE_{m0} (m =1, 3, 5, …) with approximate amplitudes of 1/m and equal phase; close to optimum when mismatch and mode coupling at the aperture is small [13]. This leads to a computationally lighter final optimization compared to more complicated optimization strategies required for the profiled horns [14]. Aperture efficiency levels above 92% have been characterized experimentally and above 95% have been calculated numerically over a frequency bandwidth of 20%. Despite the inclusion of the required building blocks (H-plane power divider, waveguide sections and bifurcation), the axial profile of the proposed antenna is relatively compact ($4.1\lambda_0$) compared to the profiled horns. Its manufacturing does not pose significant constraints although this is simpler than for profiled horns. The basic principle behind the novel horn presented here is also extensible to larger apertures where more excitation modes (TE_{n0}, $n\in\mathbb{N}^*$) propagate and should be used. This fact signifies that the proposed method could be potentially applied to radiating elements for dual-band applications. Extensibility lies also on dual-polarized design cases [20]; once the four-port square aperture radiating element is optimized, the most challenging subject relates to the excitation network, namely the four-way dual-polarized (orthomode) power divider [21], [22].

REFERENCES

[1] C. Balanis, *Antenna Theory and Design*. Hoboken, NJ, USA: Wiley, 2015.

[2] T.S. Bird and C. Granet, "*Profiled horns and feeds*", ch. 5 of L. Shafai, S. K. Sharma, and S. Rao, *Handbook of Reflector Antennas and Feed Systems: Feed Systems* (Artech House Antennas and Propagation Library), vol. 2. Norwood, MA, USA: Artech House, 2013.

[3] S. Silver, Ed., *Microwave Antenna Theory and Design*. New York: McGraw Hill, 1949.

[4] A. Rolland, M. Ettorre, M. Drissi, L Le Coq and R. Sauleau, "Optimization of reduced-size smooth-walled conical horns using BoR-FDTD and genetic algorithm", *IEEE Trans. Antennas Propag.*, vol. 58, no. 9, pp. 3094-3100, Sep. 2010.

[5] A. Rolland, A. Boriskin, Ch. Person, C. Quendo, L. Le Coq and R. Sauleau, "Lens-corrected axis-symmetrical shaped horn antenna in metalized foam with improved bandwidth", *IEEE Antennas Wireless Propag. Lett.*, vol. 11, pp. 57-60, 2012.

[6] A. Rolland, N. T. Nguyen, R. Sauleau, Ch. Person and L. Le Coq, "Smooth-walled light-weight Ka-band shaped horn antennas in metalized foam", *IEEE Trans. Antennas Propag.*, vol. 60, no. 3, pp. 1245-1251, Mar. 2012.

[7] D. Ramaccia, F. Scattone, F. Bilotti and A. Toscano, "Broadband compact horn antennas by using EPS-ENZ metamaterial lens," *IEEE Trans. Antennas Propag.*, vol. 61, no. 6, pp. 2929–2937, Jun. 2013.

[8] X. Chen and Y. Ge, "Enhancing the Radiation Performance of a Pyramidal Horn Antenna by Loading a Subwavelength Metasurface," *IEEE Access*, vol. 5, pp. 20164-20170, 2017.

[9] M. A. Koerner and R. L. Rogers, "Gain enhancement of a pyramidal horn using E- and H-plane metal baffles," *IEEE Trans. Antennas Propag.*, vol. 48, no. 4, pp. 529–538, Apr. 2000.

[10] Nasimuddin and K. P. Esselle, "A low-profile compact microwave antenna with high gain and wide bandwidth," *IEEE Trans. Antennas Propag., vol. 55, no. 6, pp. 1880–1883, Jun. 2007.*

[11] D. Sun and J. Xu, "Compact Phase Corrected H-Plane Horn Antenna Using Slow-Wave Structures," *IEEE Antennas Wireless Propag. Lett.*, vol. 16, pp. 1032-1035, 2017.

[12] J. Deng *et al*., "Horn Antenna with Miniaturized Size and Increased Gain by Loading Slow-Wave Periodic Metal Blocks," *IEEE Trans. Antennas Propag.*, vol. 69, no. 4, pp. 2365-2369, Apr. 2021.

[13] T. S. Bird and C. Granet, "Optimization of Profiles of Rectangular Horns for High Efficiency," *IEEE Trans. Antennas Propag.*, vol. 55, no. 9, pp. 2480-2488, Sept. 2007.

[14] T.S. Bird, *Fundamentals of aperture antennas*, J. Wiley & Sons Inc., Chichester, 2016.

[15] T. S. Bird and C. Granet, "Design of profiled circular horn feed with high efficiency," *Proc. IEEE Int. Symp. Antennas Propag. Soc*., pp. 1-2, Jul. 2012.

[16] A. K. Bhattacharyya and G. Goyette, "A novel horn radiator with high aperture efficiency and low cross-polarization and applications in arrays and multibeam reflector antennas," *IEEE Trans. Antennas Propag.*, vol. 52, no. 11, pp. 2850-2859, Nov. 2004.

[17] A. Cherrette, R. Parrikar and T. Smith, "High Efficiency Dual Polarized Horn Antenna," US Patent, Pub. No. US 2001/6211838 B1, Apr. 2001.

[18] J. Uher, J. Bornemann and U. Rosenberg, *Waveguide Components for Antenna Feed Systems: Theory and CAD*. Norwood, MA, USA: Artech House, 1993.

[19] Mician μWave Wizard, MICIAN GmbH. [Online]. Available: www.mician.com

[20] C. Stoumpos, J. Fraysse, G. Goussetis, R. Sauleau, C. G. González and H. Legay, "Compact and Highly Efficient Single and Dual Polarized Aperture Antennas with Integrated Multiport Overmoded Excitation," *Proc. 15th Eur. Conf. Antennas Propag. (EuCAP'21)*, pp. 1-5, Mar. 2021.

[21] C. Stoumpos, J. Fraysse, S. Tubau, G. Goussetis, R. Sauleau and H. Legay, "A Compact and Broadband Four-Way Dual Polarization Waveguide Power Divider for Antenna Arrays," *Proc. 14th Eur. Conf. Antennas Propag. (EuCAP'20)*, pp. 1-5, Mar. 2020.

[22] C. Stoumpos *et al.*, "Four-Way Orthomode Waveguide Power Dividers: Subtractive and Additive Manufacturing," *Proc. 15th Eur. Conf. Antennas Propag. (EuCAP'21),* pp. 1-5, Mar. 2021.